Magnetic correlation length in hard/soft core-shell magnetic nanoarchitectures

A. Omelyanchik*[1,2], G. Muscas[3], D. Peddis[1,2]

[1]*Department of Chemistry and Industrial Chemistry & INSTM RU, nM²-Lab, University of Genoa, 16146 Genoa, Italy*
[2]*Institute of Structure of Matter, National Research Council, nM²-Lab, Via Salaria km 29.300, Monterotondo Scalo, 00015 Rome, Italy*
[3]*Department of Physics, University of Cagliari, Cittadella Universitaria di Monserrato, S.P. 8 Km 0.700, I-09042 Monserrato (CA), Italy*

* corresponding authors: alexander.omelianchik@ext.unige.it; davide.peddis@unige.it

Abstract

The magnetic behavior of the hard/soft $CoFe_2O_4$@$NiFe_2O_4$ system is discussed within the framework of two established models for magnetic nanoparticle ensembles, the Langevin model and the Random Anisotropy Model (RAM), both of which assume coherent and spatially uniform magnetization within the magnetic volume. The proposed approach allows us to quantify how magnetic coherence develops across the structurally distinct core and shell regions and to identify the regime in which these models remain valid, as well as the conditions under which their interpretative limits emerge. In the superparamagnetic state at 300 K, the magnetic sizes extracted from Langevin fitting (~5.5 nm for the core and ~8.1 nm for the core@shell particles) are smaller than the geometric diameter, indicating partial spin disorder. Field-dependent blocking temperatures fitted using RAM yield correlation lengths $L_{corr,0} \approx 9–10$ nm, and intrinsic effective anisotropy constants $K_{eff} \approx 3.2\times10^5$ J m^{-3} for both systems. These results reveal an intrinsic limitation of coherent-rotation models when applied to core–shell architectures: the effective energy barrier represents a composite parameter that includes contributions from the core, shell, surface, and interfacial regions, which cannot be individually disentangled within a macrospin framework.

1. Introduction

Bi-magnetic nanoparticles (MNPs) with the core@shell (CS) nanoarchitecture represent a versatile class of materials in which magnetically distinct phases are exchange-coupled, enabling finely tunable and application-specific magnetic properties [1–3]. The interfacial exchange coupling between magnetically hard and soft phases enables control over key parameters such as anisotropy, surpassing the performance limits of single-phase systems. By adjusting the relative volumes of the two phases and the structural coherence at their interface, the magnetization reversal mechanisms shift from rigid coupling to spring-like behavior [4–6]. This structural and magnetic flexibility enables diverse applications, including magnetic hyperthermia, data storage, permanent magnets, and magnetoelectric composites [7–9]. Advances in seed-mediated growth methods provide precise control over the shell thickness and compositional gradients, yielding nearly single-crystalline nanoarchitectures such as $CoFe_2O_4$@$NiFe_2O_4$, Fe_3O_4@$CoFe_2O_4$, Fe_3O_4@$Zn_xCo_{1-x}Fe_2O_4$, among others [10–12].

The rapid progress in CS engineering, and in particular the ability to finely tune interfacial structure and magnetic exchange coupling across it, has also prompted a new examination of the interplay among structural length scales and magnetic behavior. In this context, the *magnetic size* has emerged as a key descriptor, bridging the structural and magnetic properties of MNPs [13–19]. While the physical diameter defines the geometric boundary of a nanoparticle typically observed by transmission electron microscopy (TEM), the magnetic size corresponds to the effective region within which local (atomic) magnetic moments are coherently aligned and contribute to the net magnetization. Disparities between these metrics arise from

non-collinear spins at the surface, lattice imperfections that disrupt exchange pathways, and magnetic interparticle interactions [20]. Saturation magnetization (M_S) is another key parameter defining the performance of any magnetic material; yet, its interpretation in MNPs is not straightforward. Numerous studies on spinel ferrite MNPs have shown that their M_S values deviate from the bulk values [19,20]. This difference is generally attributed to two main factors: (*i*) the presence of a non-collinear spin structure [20–22], (*ii*) variations in the cationic distribution in the interstitial sites of the spinel structure [23,24]. Surface spin disorder typically reduces M_S at relatively high temperatures, whereas shifts in the inversion degree may compensate for this loss or even enhance the magnetization [23,24]. Consequently, adopting bulk M_S values for nanoscale systems often leads to inconsistent interpretations, particularly when attempting to relate magnetic moment to particle volume.

The discrepancy between magnetic and physical sizes in ferrimagnetic oxides arises from disordered surface regions, where broken Fe–O–Fe superexchange bonds and reduced coordination hinder long-range spin alignment, effectively shrinking the magnetic volume [20,21,25,26]. In multi-core iron oxide nanoflowers magnetic cores form through oriented attachment with specific crystallographic relationships [27]. Magnetic sizes extracted from Langevin fits of magnetization curves $M(H)$ at 300 K closely match microstructural dimensions, showing that hierarchical structure and crystallographic coherence govern magnetic properties. However, the M_S of these nanoflowers is reduced by a ~0.5 nm disordered spin layer at the core boundaries and by inhomogeneous vacancy ordering in γ-Fe_2O_3. In other iron oxide nanoparticles, M_S reduction stems primarily from antiphase boundaries within the core with a minor contribution of a ~0.3 nm non-magnetic surface layer [28]. For instance, in iron oxide nanoparticles, the transition from a Fe_3O_4 core to a γ-Fe_2O_3 shell can create a diffuse magnetic interface despite a sharp structural boundary, as revealed by polarized small-angle neutron scattering (SANS) and micromagnetic simulations [29]. Furthermore, this magnetic boundary is not static; in $CoFe_2O_4$ MNPs, field-dependent SANS has shown that the apparent magnetic size evolves with the applied field, governed by the local competition between magnetocrystalline anisotropy, magnetostriction and Zeeman energy [30].

Although fundamental, magnetic size remains poorly quantified in bi-magnetic CS systems because experimentally separating the magnetic contributions of the core, shell, and interface is highly challenging. Conventional magnetometry provides only averaged information, while advanced techniques such as polarized SANS, XMCD, or electron holography require complex modeling [1,29–32]. Neutron-based approaches are especially powerful for separating intrinsic anisotropy and nanoscale magnetic disorder from bulk magnetometry [29,30]. These tools are rarely accessible in standard laboratories. Moreover, exchange coupling and spin canting generate diffuse magnetic boundaries rather than well-defined interfaces [1]. As a result, most studies focus primarily on tuning anisotropy and coercivity, leaving systematic quantification of magnetic size largely unexplored [8,33–35].

While intraparticle spin disorder inherently leads to a discrepancy between the physical and magnetic sizes of individual nanoparticles, the collective magnetic response of nanoparticle ensembles is further modulated by interparticle interactions. The combined influence of intra- and interparticle exchange and dipolar coupling has become a central theme in contemporary nanomagnetism, as it decisively shapes collective phenomena and functional responses [36–42]. For ensembles of interacting nanoparticles with size d well below the characteristic exchange length, spin correlations extend beyond individual particles. This forms a single magnetic unit of correlated elements with nearly uniform magnetization and an averaged magnetic response. A generalized expression describing this extended magnetic correlation length L_{corr} has been proposed [38]:

$$L_{corr} = d + \left[\frac{2 \cdot A_{eff}}{\mu_0 \cdot M_s \cdot H + C}\right]^{1/2} \quad (1)$$

where A_{eff} represents the effective intergranular exchange constant, μ_0 is the vacuum magnetic permeability ($1.2566 \cdot 10^{-6}$ T·m·A^{-1}), M_S is the saturation magnetization, H is the applied magnetic field, and C is an empirical parameter introduced to avoid divergence at $H = 0$, reflecting the variation of interaction strength with particle concentration [38]. More recently, this model has been applied to describe ensembles of single-domain MNPs with dominating dipolar interparticle interactions [41–43].

Within the RAM framework, the effective magnetic anisotropy constant (K_{eff}) represents the averaged anisotropy of N interacting units and can be expressed as:

$$K_{eff} = \frac{K^*_{eff}}{\sqrt{N}} = K^*_{eff} \cdot \left[1 + \frac{x \cdot (L^3_{corr} - d^3)}{d^3}\right]^{-1/2}, \quad (2)$$

where K^*_{eff} is the intrinsic anisotropy constant and x is the volume fraction of interacting grains. To the best of our knowledge, the RAM model has not yet been applied to bi-magnetic CS-MNPs. However, such an approach could offer valuable insight into both the collective magnetic behavior and the internal collinearity of magnetic moments in these complex nanoarchitectures. Indeed, recent studies have shown that the magnetization of CS-MNPs, specifically those with the magnetically hard core and soft shell structure, demonstrated a nonhomogeneous distribution of the magnetization [44].

The magnetically hard and soft regions in CS-MNPs exhibit distinct correlation regimes, reflecting differences in anisotropy, exchange stiffness, and structural continuity. The presence of non-collinear magnetic moments alters magnetic anisotropy and produces a pronounced temperature dependence of magnetization [45,46]. At low temperatures, this disordered region may freeze and act as a distinct magnetic phase, influencing both anisotropy and overall magnetization of the system, thus it can be magnetically active at least at low temperatures [23]. We therefore avoid the term *dead layer* in favor of non-collinear spin structure (i.e., spin canting), which better reflects the underlying physics.

In this work, we extend our previous study on $CoFe_2O_4$ (CFO) seeds and $CoFe_2O_4$@$NiFe_2O_4$ (CFO@NFO) CS-MNPs by quantifying their effective magnetic coherence lengths [47]. We estimate the magnetic size from Langevin fitting (d_{sp}) of magnetization curves and the L_{corr} using RAM. These parameters reveal how interfacial exchange coupling and interparticle interactions influence spin alignment and collective magnetic behavior. Beyond their fundamental interest, these insights provide a quantitative foundation for optimizing exchange-coupled nanoparticles in functional applications such as magnetic hyperthermia, magneto-mechanical actuation, high-density data storage, and advanced permanent-magnet architectures [48–52].

2. Samples: Synthesis and morpho-structural characterization

Cobalt ferrite ($CoFe_2O_4$, CFO) MNPs and $CoFe_2O_4$/$NiFe_2O_4$ (CFO@NFO) CS-MNPs were synthesized via a two-step high-temperature seed-mediated growth procedure under oxygen-free conditions using a Schlenk line. The synthesis route, based on the thermal decomposition of metal acetylacetonate precursors in the presence of oleic acid, oleylamine, and benzyl ether, was reported elsewhere [47]. The method ensures the formation of monodisperse CFO seeds subsequently employed for the growth of the NFO shell under controlled reflux conditions.

X-ray diffraction (XRD) patterns were recorded with a Bruker DaVinci2 diffractometer using Cu Kα radiation (λ = 1.5406 Å) in Bragg–Brentano (θ–2θ) geometry over the 10°–75° 2θ range. The mean crystallite size was estimated from the Scherrer equation ($d_{XRD} = 0.9\lambda/\beta \cos\theta$), using the full width at half maximum (β) of the 5 most intense reflections [53]. Particle morphology and size distribution were analyzed by Hitachi S5500 scanning transmission electron microscopy (TEM) operating at 30 kV. The particle size distribution was fitted with a log-normal function, yielding the median diameter (d_{TEM}). Magnetic characterization was performed with a Quantum Design SQUID magnetometer up to $\mu_0 H$ = 5 T in the 5–300 K range. Results of magnetic measurements are available online [54].

XRD patterns confirmed that both CFO and CFO@NFO MNPs crystallize in the cubic spinel structure, with no detectable secondary phases (Figure 1a). Due to the close lattice parameters of $CoFe_2O_4$ and $NiFe_2O_4$, the individual phases could not be resolved by conventional powder XRD and STEM (Figure 1b). The observed reflection broadening and increased structural coherence length in the CS-samples indicate epitaxial growth of the NFO shell on the CFO core. According to STEM analysis, the CS-MNPs were larger than their corresponding CFO seed particles, consistent with the formation of a ~2 nm shell, as also supported by XRD results. Average sizes obtained by both methods are reported in Table 1. Complete details of the synthesis procedure, basic magnetic and structural characterization are described in our previous work [47].

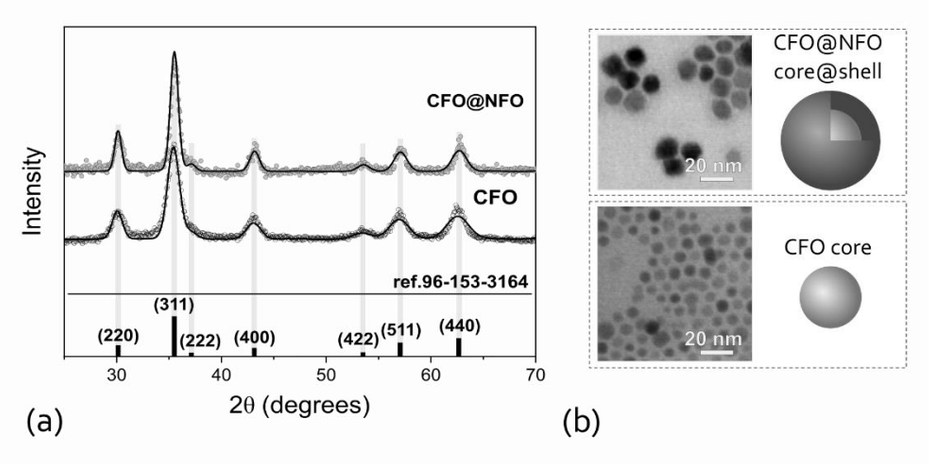

Figure 1. (a) XRD patterns and (b) TEM images of CFO and CFO@NFO MNPs.

Table 1. Structural and magnetic parameters of the samples at 300 K: d_{XRD} and d_{TEM} – the average volume-weighted crystallite and particle sizes, respectively; M_S – the saturation magnetization; $\mu_0 H_a$ – the anisotropy field; K_{eff}^{LAS} – the effective anisotropy constant, and χ_d – the high-field magnetic susceptibility. Uncertainties are given in parentheses.

Sample	d_{XRD}, **nm**	d_{TEM}, **nm**	$M_{S,b}$, **A·m²·kg⁻¹**	$\mu_0 H_a$, **T**	K_{eff}^{LAS}, **kJ·m⁻³**	χ_d, **A·m²·kg⁻¹·T⁻¹**
CFO	6.2(2)	7.1(1)	74(3)	1.7(1)	327(33)	0.40(1)
CFO@NFO	9.2(4)	12(1)	68(2)	0.68(4)	120(21)	0.39(1)

3. Magnetic saturation, size, and anisotropy

Single-domain MNPs exhibit two limiting regimes depending on temperature and anisotropy energy [37,55,56]. When the thermal energy is sufficient to overcome the anisotropy barrier within the experimental timescale, the magnetic moment of each particle undergoes rapid fluctuations. Under these conditions, the system is in the superparamagnetic regime, characterized by zero coercivity ($H_C = 0$) and remanence ($M_R = 0$). The term *superparamagnetic* reflects the fact that magnetization reversal occurs freely through thermal activation, without being hindered by the anisotropy energy barrier. At lower temperatures, thermal fluctuations become insufficient to overcome the anisotropy energy barrier, individual magnetic moments become blocked, and the system behaves like an ensemble of quasi-static single-domain magnets. The transition between these regimes is characterized by the so-called blocking temperature (T_B), which depends on particle volume, effective magnetic anisotropy, and the experimental measurement time [55,57]. Within this framework, the analysis of blocked/superparamagnetic states provides direct access to magnetic size, anisotropy, and collective effects.

As shown in Figure 2a, the field dependence of the magnetization of samples measured at 300 K display superparamagnetic-like behavior with negligible H_C and M_R/M_S, indicating that all samples are

superparamagnetic at room temperature. For an ensemble of single-domain particles with randomly distributed easy axes, the high-field region of *M(H)* loop can be fitted with the law of approach to saturation (LAS)

$$M(H)|_{H\gg H_{irr}} = M_{S,b}\cdot\left[1-\frac{1}{15}\cdot\left(\frac{H_a}{H}\right)^2\right]+\mu_0\cdot\chi_d\cdot H, \quad (3)$$

where $M_{S,b}$ denotes the saturation magnetization of magnetically ordered phase, H_a – anisotropy field, related to anisotropy constant, and χ_d – susceptibility at high field, which can be attributed to the non-collinear spin structure due to competing interactions between sublattices, and to the symmetry breaking at the particle surface [58–60]. To perform the LAS fits, the high-field window was systematically adjusted in the range from 0.7 to 5 T (Figure S1). We find that M_S exhibits remarkable stability, varying by less than 5% across all tested high-field ranges (70–74 Am²/kg for CFO and 68–69 Am²/kg for CFO@NFO). This high stability demonstrates that the data density in the high-field regime is entirely sufficient to yield robust values for M_S. In contrast, H_a is inherently more sensitive to the choice of fitting range. Specifically, H_a varies from 1.7 to 1.1 T for CFO and from 0.70 to 0.62 T for CFO@NFO as the lower bound of the fit is adjusted. Based on the analysis of the goodness of fit parameter χ^2 (Figure S1), the interval from 2 to 5 T was selected as the optimal high-field fitting range. The corresponding magnetic parameters obtained from the LAS fits in the 2–5 T range are summarized in Table 1. The experimentally derived M_S values are slightly lower than those of bulk (volume-averaged estimates for the CS-system).

The equilibrium magnetization of MNPs above the blocking temperature (T_B) can be described using the Langevin function, assuming a distribution of particle magnetic moments $\mu = M_S{\cdot}V$ that follows a log-normal size distribution. In this approach, the total magnetization $M(H)$ of an ensemble of non-interacting particles is obtained by integrating the Langevin function $L(\alpha)$ over all particle sizes [14,61]:

$$M(H) = M_S\cdot\int_0^\infty L(\alpha)\cdot P(\mu)\,d\mu, \quad (4)$$

where $P(\mu)$ is the normalized log-normal distribution:

$$P(\mu) = \frac{1}{\mu\cdot w\cdot\sqrt{2\pi}}\cdot e^{-\frac{[ln(\mu/<\mu>)]^2}{2w^2}}. \quad (5)$$

Here $<\mu>$ is the median magnetic moment of particles in the superparamagnetic regime, and w – the width parameter of the distribution. The Langevin function $L(\alpha)$ is defined as [14,61]:

$$L(\alpha) = coth(\alpha)-\frac{1}{\alpha} \quad (6)$$

with

$$\alpha = \frac{\mu_0\cdot\mu\cdot H}{k_B\cdot T}, \quad (7)$$

where k_B – the Boltzmann constant, and T – the absolute temperature.

Figure 2a shows $M(H)$ curves measured at 300 K and fitted with the Langevin function, considering a log-normal distribution to determine magnetic size distribution parameters $<\mu>$ and w. As discussed in the following sections, the blocking temperature (T_B) for both systems is well below 300 K; consequently, the thermal energy k_BT substantially exceeds the magnetic anisotropy energy KV at room temperature, placing both samples in the superparamagnetic regime within the Néel–Brown model [62,63]. Regarding interparticle interactions, dipolar coupling is limited by the dispersion of particles in a non-magnetic medium and by the ~2 nm oleic acid surfactant coating, which enforces a minimum interparticle separation [47]. While dipolar interactions cannot be entirely excluded, we expect them to introduce only a minor perturbation to the superparamagnetic response at 300 K.

In Langevin analysis, the M_S in Eq. (4) can be treated as a free fitting parameter. For the CFO seed MNPs, the fit with M_S treated as a free parameter yielded a value consistent with the LAS ($M_{S,L}$ = 77±2 A·m²·kg^{-1}) with

an average moment $<\mu>$ = 5.0(2)×10^3 μ_B. In contrast, leaving M_S free for the CFO@NFO CS-sample produced an unphysically high value ($M_{S,L}$ = 90±15 A·m^2·kg^{-1}), accompanied by large parameter uncertainties, a symptom of over-parameterization in a system where M_S and $<\mu>$ are correlated in the fitting landscape. The extracted average magnetic moment $<\mu>$ = 16(4)×10^3 μ_B is approximately three times higher than that of the CFO seeds. This proportional increase is consistent with the expected growth of the magnetic volume, since the physical volume of the CFO@NFO particles is roughly 3–4 times larger than that of the CFO cores.

To resolve the ambiguity in the fit, M_S was fixed to the values determined independently from the LAS. It is important to emphasize that this constraint does not predetermine the magnetic size: the median moment $<\mu>$ is mostly governed by the shape and curvature of the $M(H)$ curve and is extracted independently of M_S. The M_S enters the subsequent geometric conversion, fixing it reduces the number of free parameters and stabilizes the fit without introducing circularity in the determination of d_{sp}. The resulting average magnetic moments are 5.2(2)×10^3 μ_B and 12(1)×10^3 μ_B for CFO and CFO@NFO, respectively. Assuming spherical geometry and expressing the magnetic moment in A·m^2, the corresponding magnetic diameter of superparamagnetic particles (d_{sp}) can be calculated as

$$d_{sp} = \left(\frac{6}{\pi} \cdot \frac{<\mu>}{M_{S,b}}\right)^{1/3}. \qquad (8)$$

Converting $<\mu>$ to a magnetic diameter requires a physically appropriate value of $M_{S,b}$. For composite nanoparticles, a nominal bulk reference is often unavailable or not meaningful, as the effective magnetization depends on phase composition, cation distribution, and interfacial disorder [28,34]. The LAS fit provides a reliable alternative: by explicitly separating the ordered-spin contribution $M_{S,b}$ from the non-collinear surface term $\chi_d \cdot H$, it yields the intrinsic magnetization of the ferrimagnetically ordered volume. Using this $M_{S,b}$, d_{sp} then represents the diameter of the coherently magnetized region. The d_{sp} obtained from the Langevin fitting were ~5.5 nm for the CFO sample and ~8.1 nm for CFO@NFO, when the $M_{S,b}$ values from LAS fit are used to represent the magnetically ordered core. For comparative purposes, we also adopt slightly higher M_S values representative of bulk materials: 80 A·m^2·kg^{-1} for CFO and 60 A·m^2·kg^{-1} for CFO/NFO (the latter being a rough approximation due to the lack of precise bulk data for the composite system). Under these assumptions, the corresponding magnetic diameters are ~5.3 nm and ~8.5 nm, respectively. These values follow the same trend as the d_{XRD} and d_{TEM}, though they are systematically smaller ($d_{SP} < d_{XRD} < d_{TEM}$), as expected when comparing magnetic and geometric dimensions (Figure S2).

While the Langevin formalism successfully captures the overall superparamagnetic behavior, the visible deviations in the intermediate-field region for the CFO sample arise from physical mechanisms neglected by the ideal, single-size Langevin model. Specifically, cobalt ferrite is characterized by a high magnetocrystalline anisotropy that partially limits thermally induced moment rotation under an applied field. Additionally, the combined effects of size polydispersity and weak interparticle dipolar interactions within the ensemble shear the magnetization curve, thereby slowing the approach to saturation relative to the ideal, non-interacting isotropic model [19].

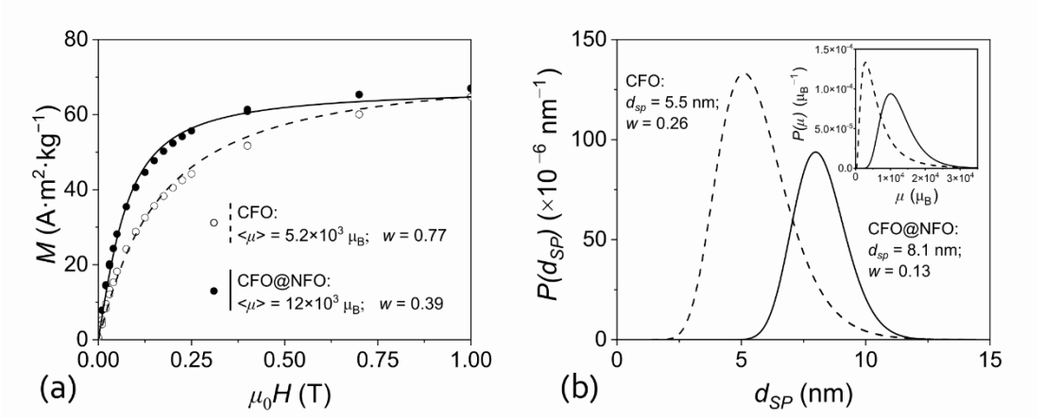

Figure 2. (a) $M(H)$ curves measured at 300 K for CFO (empty symbols) and CFO@NFO (full symbols) samples. Fit with the Langevin function considering the log-normal distribution of magnetic moments is shown by lines, and the resulting parameters are indicated. (b) Distributions of the d_{SP} corresponding to the fits in panel (a); the inset shows normalized to unity of the area of the distribution of corresponding magnetic moments.

3. 1 Intrinsic anisotropy and coherence length in CS-MNPs

The temperature dependence of magnetization was studied using zero-field-cooled (ZFC) and field-cooled (FC) protocols [37]. In the ZFC procedure, the sample was cooled from 300 K to 5 K in a zero magnetic field, after which a static field H was applied. $M_{ZFC}(T)$ was measured during heating to 300 K, and $M_{FC}(T)$ was recorded during subsequent cooling. This procedure was repeated for a set of magnetic fields ranging from 2.5 mT up to 100 mT. Figure 3 shows the $M_{ZFC}(T)$ and $M_{FC}(T)$ curves for CFO and CFO@NFO samples, which exhibit markedly different temperature dependences between the two systems.

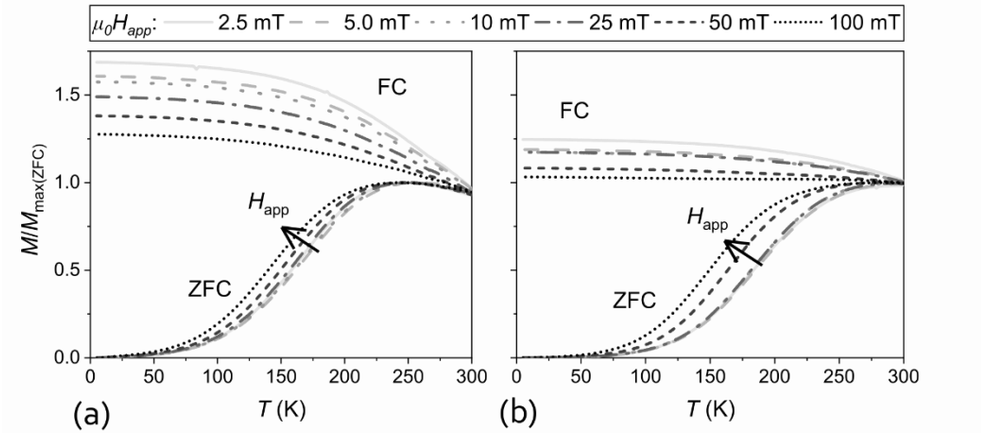

Figure 3. $M_{ZFC}(T)$ and $M_{FC}(T)$ curves measured at various fields for (a) CFO and (b) CFO@NFO samples.

According to the Néel–Brown model, the thermal relaxation of a nanoparticle's magnetic moment occurs by overcoming an energy barrier $E_a = K_{eff} \cdot V$. Since real systems contain particles with a distribution of sizes and anisotropies, they exhibit a corresponding distribution of energy barriers. The average blocking temperature T_B marks the condition where $E_a \approx k_B \cdot T$, meaning that approximately half of the particles remain magnetically blocked while the other half is in the superparamagnetic regime [37,64]. The distribution of magnetic energy barriers is then proportional to the first derivative of the thermoremanent magnetization ($M_{TRM} \approx M_{FC} - M_{ZFC}$) (Figure S3) [65]:

$$f(\Delta E) \propto \frac{d(M_{FC} - M_{ZFC})}{dT} \equiv f(T_B). \qquad (9)$$

The average blocking temperature (T_B) was determined as a temperature where the cumulative integral of the $f(T_B)$ reaches 50% of its maximum value [57]. It should be noted that in core–shell nanoparticles, the energy barrier extracted within the Néel–Brown framework represents a single effective term (i.e., $K_{eff} = K_{core} + K_{shell}$)which also encompasses contributions from the surface and interfacial regions [66]. Deconvolving individual contributions for different phases is non-trivial from experimentally observed energy landscapes.

Interestingly, the average blocking temperature T_B remains nearly identical for both samples, with a difference that changes from 7% to 1% from minimal to maximal applied field (Figure 4). Since $T_B \propto K_{eff} \cdot V$, the average magnetic volume and effective anisotropy can be estimated from the field dependence of T_B using the expression [37]:

$$T_B(H) = \frac{K_{eff} V}{k_B \cdot \ln(\tau_m/\tau_0)} \left[1 - \frac{\mu_0 H}{\mu_0 H_a}\right]^{1.5}, \qquad (10)$$

where $\mu_0 H_a = 2 \cdot K_{eff}/M_S$ is the Stoner–Wohlfahrt anisotropy field, τ_m = 60 s can be considered as the typical experimental time in DC magnetization measurements and $\tau_0 = 10^{-11}$ s for ferromagnetic particles. As the values and general trend of field dependence of T_B for core and CS systems are quite similar, the calculated values of particles size and effective magnetic anisotropy constants are similar as well (d = 8.2(8) nm, K_{eff} = 210(20) kJ·m^{-3} for CFO and d = 9.6(9) nm, K_{eff} = 140(10) kJ·m^{-3} for CFO@NFO). Notably, these variations are much smaller than expected from geometric size differences and simple volume-averaging of anisotropy. A plausible explanation is that interparticle magnetic interactions modify the field dependence of T_B, an effect that can be incorporated within the RAM [39,42]:

$$T_B(H) = \frac{K^*_{eff} \cdot V_N}{k_B \cdot \ln(\tau_m/\tau_0)} \left[1 - \frac{\mu_0 H}{\mu_0 H^N_a}\right]^{1.5}, \qquad (11)$$

where K^*_{eff} is the effective magnetic anisotropy constant over N interacting particles, occupying volume $V_N = \pi/6 \cdot [d^3 + x \cdot (L^3_{corr} - d^3)]$.

The field dependence of the T_B is presented in Figure 4, and the fitting parameters extracted from $T_B(H)$ using eq. 11 are summarized in Table 2. A critical aspect in applying RAM is the choice of the internal magnetic length scale d. When the physical diameter d_{TEM} of the CFO@NFO particles is used, the fit does not converge. This indicates that the effective magnetic volume participating in coherent relaxation is smaller than the geometric size of the CS-MNPs. Because magnetic anisotropy is dominated by the CFO core, we therefore take d equal to the CFO core diameter for both samples when applying the RAM analysis.

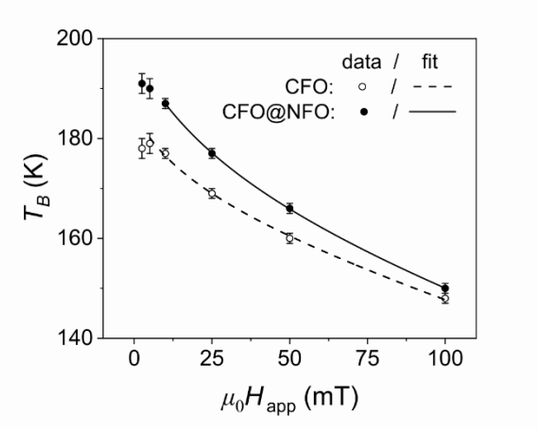

Figure 4. Field dependence of mean blocking temperature for CFO (empty symbols) and CFO@NFO (full symbols). Lines indicate fit with RAM (**eq. 10**).

The intrinsic effective anisotropy constants from the RAM analysis are almost equal, within experimental error, for both samples (K^*_{eff} = 326(4) kJ·m^{-3} for CFO and 319(1) kJ·m^{-3} for CFO@NFO) and align with the first-order magnetocrystalline anisotropy of cobalt ferrite (K_1 = 290 kJ·m^{-3} [67]), consistent with a hard-core–dominated response. Although increased K_{eff} is frequently reported for small $CoFe_2O_4$ MNPs due to surface spin canting and broken symmetry [60,68,69], this surface contribution is significantly minimized in high-crystallinity nanoparticles synthesized via high-temperature thermal decomposition. Consequently, the magnetic anisotropy in CFO is predominantly governed by the intrinsic magnetocrystalline contribution [32,70]. For the CFO sample, K^*_{eff} matches the anisotropy constant estimated at 300 K from the LAS fit, while it is ~3 times higher for CFO@NFO sample (**Table 1**). This discrepancy may arise because the Stoner–Wohlfarth-based LAS model assumes non-interacting, single-phase coherent rotation, while neglecting relaxation processes. In the exchange-coupled CFO@NFO CS system, however, the soft-magnetic NFO shell facilitates magnetization rotation, resulting in a significantly reduced volume-averaged effective anisotropy under high-field LAS fitting, whereas the RAM analysis remains highly sensitive to the local, core-dominated exchange correlation length.

The correlation lengths at zero field are similarly comparable for the two systems ($L_{corr,0}$ = 9(1) nm for CFO and 10(1) nm for CFO@NFO), both remaining close to the CFO core diameter. The observed similarity of $L_{corr,0}$ to the core size could arise from (i) the hard core dominating the energy barrier even if the shell is partially coherent, (ii) a distribution of shell thickness/anisotropy leading to an effective barrier dominated by the core, or (iii) model assumptions (single effective K_{eff}*, single L_{corr}, and d=d_{core} assumption) that average out shell contributions.

These conclusions are supported by the intrinsic blocking temperatures T^*_B: in a simple additive-barrier picture, adding a magnetically active shell should increase the effective energy barrier, considering preservation of the core. The experimental observation that T^*_B remains essentially unchanged between systems (~160 K for CFO and 157 K for CFO@NFO), phenomenologically can be explained as the NFO shell does not measurably contribute to the barrier extracted from the $T_B(H)$ analysis, i.e., the soft shell does not participate in the coherently relaxing magnetic unit described by the macrospin model.

The larger A_{eff} for CFO@NFO (6.4(7)×10^{-14} J·m^{-1} vs. 1.5(7)×10^{-14} J·m^{-1} for core) is consistent with stronger interparticle dipolar coupling, expected from the approximately threefold increase in magnetic moment per particle, since $E_{dip} \propto \mu^2$, as it was already discussed [47]. An additional geometric contribution arises from the reduced relative interparticle separation for larger particles with a fixed surfactant layer thickness. However, we note that forcing d=d_{core} in the RAM fit for CFO@NFO introduces a parameter ambiguity: the model cannot fully distinguish between a genuine increase in interaction strength and an artifact of the constrained reference length scale. The value of A_{eff} for the CS-system should therefore be treated as a phenomenological indicator of enhanced interparticle coupling rather than a quantitative absolute measure.

Table 2. Derived magnetic properties: d_{sp} – magnetic diameter from Langevin fit, $L_{corr,0}$, is the magnetic correlation length at zero magnetic field from the RAM, K^*_{eff} – the intrinsic effective magnetic anisotropy constant, T^*_B is the intrinsic blocking temperature, and A_{eff} is the effective exchange stiffness constant. Uncertainties are given in parentheses.

Sample	d_{sp}, **nm**	$L_{corr,0}$, **nm**	K^*_{eff}, **kJ·m^{-3}**	T^*_B, **K**	A_{eff}, **10^{-14} J·m^{-1}**
CFO	5.5(5)	9(1)	326(4)	160(2)	1.5(7)
CFO@NFO	8.1(8)	10(1)	319(1)	157(2)	6.4(7)

Interestingly, the $L_{corr,0}$ values show a behavior that differs from the d_{sp} obtained from the Langevin fit. Both RAM and Langevin fit approaches provide information on the magnetic size. However, the first relies on

the analysis of phenomena governed by the equilibrium of the anisotropy energy ($E_a = K_{eff} \cdot V$) vs. temperature. The latter investigates the equilibrium between the Zeeman ($E_z = H \cdot M_S \cdot V$) and the thermal energy. Hence, the difference in characteristic lengths $L_{corr,0}$ and d_{sp} may originate from a combination of factors such as the temperature dependence of K_{eff}, anisotropy dispersion for particles of different sizes in distribution, or consideration of clusterization in the RAM model. The estimated magnetic size of both the systems investigated does not overcome the physical size of two particles ($2 \times d_{TEM}$), considered as a limit for long-range collective states [42]. Thus, the magnetic behavior of both samples is determined by the intrinsic magnetic anisotropy within the non-interacting model [40].

The Néel–Brown formalism — even when extended within the RAM framework — rests on the assumption of coherent, uniform magnetization rotation within a macrospin. This assumption becomes progressively less valid in exchange-coupled core–shell architectures, where the magnetically soft shell may undergo non-uniform or spring-like reversal driven by competing exchange interactions. In such cases, the reversal is not governed by a single energy barrier but by a more complex energy landscape that explicitly includes the interfacial exchange coupling energy. This interpretation remains speculative, and further experimental and theoretical studies are required to clarify the origin of this discrepancy.

Recent studies have revealed that CS-MNPs may exhibit complex and unconventional magnetic structures. For instance, polarized small-angle neutron scattering combined with atomistic simulations on $Fe_3O_4/Mn_xFe_{3-x}O_4$ systems demonstrated that the spin canting extends throughout the entire particle rather than being confined to the surface, driven by the Dzyaloshinskii–Moriya interaction [34]. Moreover, this frustrated magnetic configuration can give rise to multiparticle coherent spin canting under an applied field. Theoretical works have further suggested that magnetically soft shells can behave as screening layers, forming demagnetizing-like spin textures [44]. Song and Zhang [71] showed that reversing the order of soft and hard phases in CS-architectures leads to pronounced changes in magnetic anisotropy, likely associated with different coherent rotation mechanisms. An enhancement of magnetic anisotropy in hard@soft configurations relative to their soft@hard counterparts was also confirmed in our previous study [47]. Taken together, these findings, along with our present observation of an unexpectedly preserved L_{corr} and the intrinsic effective magnetic anisotropy K^*_{eff}, indicate that hard@soft MNPs represent a distinct class of magnetically correlated nanostructures, warranting further detailed investigation.

4. Conclusions

This work focuses on the magnetic correlations across the interface of hard@soft CS-MNPs. $CoFe_2O_4$@$NiFe_2O_4$ nanoparticles with a narrow size distribution were selected as a model system for a well-defined exchange-coupled nanoarchitecture. The quantitative evaluation of the magnetic correlation length obtained from the RAM analysis reveals that the $CoFe_2O_4$@$NiFe_2O_4$ heterostructure preserves essentially the same magnetic coherence scale and intrinsic anisotropy as the magnetically hard $CoFe_2O_4$ core. Although the physical particle size increases with the growth of the $NiFe_2O_4$ shell, the correlation length extracted from RAM does not extend beyond that of the core, indicating that coherent magnetization does not propagate through the soft shell probed by this analysis for hard@soft MNPs. The comparison between the magnetic size derived from Langevin analysis and the correlation length from RAM highlights their complementary nature. The former reflects the thermally active magnetic volume, whereas the latter traces the spatial extent of ferro(i)magnetic coherence.

This inference must be interpreted within the limitations of the Néel–Brown/RAM macrospin framework. Both approaches treat the relaxing entity as a single coherently magnetized unit with an effective anisotropy barrier, and thus cannot represent incoherent magnetization textures, interfacial spin frustration, or exchange-spring–like modes in the soft shell [44,52]. In the "inactive shell" conclusion is thus phenomenological: the shell does not contribute to the effective barrier extracted from $T_B(H)$, but it may still

participate in reversal through non-uniform processes that lie outside the model's degrees of freedom. A more complete description would require spatially resolved (micromagnetic) modeling beyond a uniform-rotation picture.

This picture is consistent with the current state of the art, as confirmed by SANS, Monte Carlo mesoscale and micromagnetic simulations [29,30,66]. Real interfaces in bi-magnetic CS-MNPs can extend over several nanometers, forming chemically, structurally, and magnetically graded regions. Our results support a shift toward a center–periphery model: the magnetic identity of the nanoparticle develops progressively from the core toward the outer region rather than being partitioned into two idealized domains. This framework, which will be described in detail in future work, reflects how structural coherence, interfacial exchange, and local spin disorder collectively shape magnetic correlations across the entire nanoarchitecture.

Supplementary material

Figure S1: Magnetization versus magnetic field, $M(H)$, measured at 300 K for CFO and CFO@NFO samples. **Figure S2**: Distributions of the magnetic particle size estimated from Langevin fit of $M(H)$ dependencies at 300 K and histograms of physical particle size distribution measured with TEM for CFO and CFO@NFO samples. **Figure S3**: The first derivatives $dM_{TRM}/dT = d(M_{FC} - M_{ZFC})/dT$ at various measuring magnetic fields for CFO and CFO@NFO samples.

Conflict of Interest

The authors have no conflicts to disclose.

DATA AVAILABILITY

The data that support the findings of this study are openly available in Zenodo, at 10.5281/zenodo.17941186, reference number 54.

References

1. López-Ortega, A.; Estrader, M.; Salazar-Alvarez, G.; Estradé, S.; Golosovsky, I. V.; Dumas, R.K.; Keavney, D.J.; Vasilakaki, M.; Trohidou, K.N.; Sort, J.; et al. Strongly Exchange Coupled Inverse Ferrimagnetic Soft/Hard, MnxFe3−xO4/FexMn3−xO4, Core/Shell Heterostructured Nanoparticles. *Nanoscale* **2012**, *4*, 5138, doi:10.1039/c2nr30986f.
2. Chai, Y.; Lou, Q.; Xu, M.; Hong, S.; Feng, F.; Liu, Y.; Li, Q.; Feng, X.; Xiao, H.; Chen, A.; et al. Modulation of Magnetic Exchange Coupling via Constructing Bi- or Multimagnetic Heterointerfaces. *J. Phys. Chem. Lett.* **2022**, *13*, 12082–12089, doi:10.1021/acs.jpclett.2c02922.
3. Sartori, K.; Choueikani, F.; Gloter, A.; Begin-Colin, S.; Taverna, D.; Pichon, B.P. Room Temperature Blocked Magnetic Nanoparticles Based on Ferrite Promoted by a Three-Step Thermal Decomposition Process. *J. Am. Chem. Soc.* **2019**, *141*, 9783–9787, doi:10.1021/jacs.9b03965.
4. Viñas, S.L.; Simeonidis, K.; Li, Z.-A.; Ma, Z.; Myrovali, E.; Makridis, A.; Sakellari, D.; Angelakeris, M.; Wiedwald, U.; Spasova, M.; et al. Tuning the Magnetism of Ferrite Nanoparticles. *J. Magn. Magn. Mater.* **2016**, *415*, 20–23, doi:10.1016/j.jmmm.2016.02.098.
5. Silva, F.G. da; Vasilakaki, M.; Cabreira Gomes, R.; Aquino, R.; Campos, A.F.C.; Dubois, E.; Perzynski, R.; Depeyrot, J.; Trohidou, K. A Numerical Study on the Interplay between the Intra-Particle and Interparticle Characteristics in Bimagnetic Soft/Soft and Hard/Soft Ultrasmall Nanoparticle Assemblies. *Nanoscale Adv.* **2022**, *4*, 3777–3785, doi:10.1039/D1NA00894C.
6. Estrader, M.; López-Ortega, A.; Estradé, S.; Golosovsky, I. V.; Salazar-Alvarez, G.; Vasilakaki, M.; Trohidou, K.N.; Varela, M.; Stanley, D.C.; Sinko, M.; et al. Robust Antiferromagnetic Coupling in Hard-Soft Bi-Magnetic Core/Shell Nanoparticles. *Nat. Commun.* **2013**, *4*, 2960, doi:10.1038/ncomms3960.
7. López-Ortega, A.; Estrader, M.; Salazar-Alvarez, G.; Roca, A.G.; Nogués, J. Applications of Exchange

Coupled Bi-Magnetic Hard/Soft and Soft/Hard Magnetic Core/Shell Nanoparticles. *Phys. Rep.* **2015**, *553*, 1–32, doi:10.1016/j.physrep.2014.09.007.

8. Zhang, Q.; Castellanos-Rubio, I.; Munshi, R.; Orue, I.; Pelaz, B.; Gries, K.I.; Parak, W.J.; Del Pino, P.; Pralle, A. Model Driven Optimization of Magnetic Anisotropy of Exchange-Coupled Core-Shell Ferrite Nanoparticles for Maximal Hysteretic Loss. *Chem. Mater.* **2015**, *27*, 7380–7387, doi:10.1021/acs.chemmater.5b03261.
9. Song, H.; Listyawan, M.A.; Ryu, J. Core–Shell Magnetoelectric Nanoparticles: Materials, Synthesis, Magnetoelectricity, and Applications. *Actuators* **2022**, *11*, 1–20, doi:10.3390/act11120380.
10. Omelyanchik, A.; Villa, S.; Locardi, F.; Ferretti, A.M.; Ponti, A.; Singh, G.; Barucca, G.; Slimani, S.; Del Tedesco, A.; Riello, P.; et al. Magnetic Anisotropy and Interactions in Hard/Soft Core/Shell Nanoarchitectures: The Role of Shell Thickness. *Chem. Mater.* **2024**, doi:10.1021/acs.chemmater.4c01421.
11. Phong, L.T.H.; Manh, D.H.; Thanh, T.D.; Bach, T.N.; Ky, V.H.; Skorvanek, I.; Kovac, J.; Svec, P.; Phan, T.-L.; Phan, M.H. Contrasting Shell Thickness-Dependent Magnetic Behaviors of CoFe2O4@Fe3O4 and Fe3O4@CoFe2O4 Core/Shell Nanoparticles. *J. Alloys Compd.* **2024**, *1005*, 176138, doi:10.1016/j.jallcom.2024.176138.
12. Fabris, F.; Lohr, J.; Lima, E.; de Almeida, A.A.; Troiani, H.E.; Rodríguez, L.M.; Vásquez Mansilla, M.; Aguirre, M.H.; Goya, G.F.; Rinaldi, D.; et al. Adjusting the Néel Relaxation Time of Fe 3 O 4 /Zn x Co 1− x Fe 2 O 4 Core/Shell Nanoparticles for Optimal Heat Generation in Magnetic Hyperthermia. *Nanotechnology* **2021**, *32*, 065703, doi:10.1088/1361-6528/abc386.
13. Unni, M.; Uhl, A.M.; Savliwala, S.; Savitzky, B.H.; Dhavalikar, R.; Garraud, N.; Arnold, D.P.; Kourkoutis, L.F.; Andrew, J.S.; Rinaldi, C. Thermal Decomposition Synthesis of Iron Oxide Nanoparticles with Diminished Magnetic Dead Layer by Controlled Addition of Oxygen. *ACS Nano* **2017**, *11*, 2284–2303, doi:10.1021/acsnano.7b00609.
14. Chantrell, R.W.; Popplewell, J.; Charles, S.W. Measurements of Particle Size Distribution Parameters in Ferrofluids. *IEEE Trans. Magn.* **1978**, *14*, 975–977, doi:10.1109/TMAG.1978.1059918.
15. Berkov, D. V.; Görnert, P.; Buske, N.; Gansau, C.; Mueller, J.; Giersig, M.; Neumann, W.; Su, D. New Method for the Determination of the Particle Magnetic Moment Distribution in a Ferrofluid. *J. Phys. D. Appl. Phys.* **2000**, *33*, 331–337, doi:10.1088/0022-3727/33/4/303.
16. Gerina, M.; Angotzi, M.S.; Mameli, V.; Gajdošová, V.; Rainer, D.N.; Dopita, M.; Steinke, N.-J.; Aurélio, D.; Vejpravová, J.; Zákutná, D. Size Dependence of the Surface Spin Disorder and Surface Anisotropy Constant in Ferrite Nanoparticles. *Nanoscale Adv.* **2023**, *5*, 4563–4570, doi:10.1039/d3na00266g.
17. Neumann, S.; Kuger, L.; Arlt, C.R.; Franzreb, M.; Rafaja, D. Influence of the Hierarchical Architecture of Multi-Core Iron Oxide Nanoflowers on Their Magnetic Properties. *Sci. Rep.* **2023**, *13*, 5673, doi:10.1038/s41598-023-31294-4.
18. Maltoni, P.; Varvaro, G.; Abdolrahimi, M.; Peddis, D.; Mathieu, R. Time and Temperature Dependent Magnetic Particles. *J. Appl. Phys.* **2023**, doi:10.1063/5.0144701.
19. Bender, P.; Balceris, C.; Ludwig, F.; Posth, O.; Bogart, L.K.; Szczerba, W.; Castro, A.; Nilsson, L.; Costo, R.; Gavilán, H.; et al. Distribution Functions of Magnetic Nanoparticles Determined by a Numerical Inversion Method. *New J. Phys.* **2017**, *19*, doi:10.1088/1367-2630/aa73b4.
20. Batlle, X.; Moya, C.; Escoda-Torroella, M.; Iglesias, Ò.; Fraile Rodríguez, A.; Labarta, A. Magnetic Nanoparticles: From the Nanostructure to the Physical Properties. *J. Magn. Magn. Mater.* **2022**, *543*, 168594, doi:10.1016/j.jmmm.2021.168594.
21. Heber, G.; Goedsche, F. A Remark on "Dead Layers" in Magnetic Thin Films. *Czechoslov. J. Phys.* **1971**, *21*, 1121–1122, doi:10.1007/BF01690926.
22. Vázquez-Vázquez, C.; López-Quintela, M.A.; Buján-Núñez, M.C.; Rivas, J. Finite Size and Surface Effects on the Magnetic Properties of Cobalt Ferrite Nanoparticles. *J. Nanoparticle Res.* **2011**, *13*, 1663–1676, doi:10.1007/s11051-010-9920-7.
23. Peddis, D.; Cannas, C.; Piccaluga, G.; Agostinelli, E.; Fiorani, D. Spin-Glass-like Freezing and Enhanced Magnetization in Ultra-Small CoFe 2 O 4 Nanoparticles. *Nanotechnology* **2010**, *21*, 125705, doi:10.1088/0957-4484/21/12/125705.
24. Mameli, V.; Musinu, A.; Ardu, A.; Ennas, G.; Peddis, D.; Niznansky, D.; Sangregorio, C.; Innocenti, C.; Thanh, N.T.K.; Cannas, C. Studying the Effect of Zn-Substitution on the Magnetic and Hyperthermic Properties of Cobalt Ferrite Nanoparticles. *Nanoscale* **2016**, *8*, 10124–10137, doi:10.1039/C6NR01303A.
25. Respaud, M.; Broto, J.M.; Rakoto, H.; Fert, A.R.; Thomas, L.; Barbara, B.; Verelst, M.; Snoeck, E.; Lecante, P.; Mosset, A.; et al. Surface Effects on the Magnetic Properties of Ultrafine Cobalt Particles. *Phys. Rev. B* **1998**, *57*, 2925–2935, doi:10.1103/PhysRevB.57.2925.
26. Muscas, G.; Congiu, F.; Concas, G.; Cannas, C.; Mameli, V.; Yaacoub, N.; Hassan, R.S.; Fiorani, D.; Slimani, S.; Peddis, D. The Boundary Between Volume and Surface-Driven Magnetic Properties in Spinel Iron

Oxide Nanoparticles. *Nanoscale Res. Lett.* **2022**, *17*, doi:10.1186/s11671-022-03737-w.
27. Neumann, S.; Kuger, L.; Arlt, C.R.; Franzreb, M.; Rafaja, D. Influence of the Hierarchical Architecture of Multi-Core Iron Oxide Nanoflowers on Their Magnetic Properties. *Sci. Rep.* **2023**, *13*, 1–15, doi:10.1038/s41598-023-31294-4.
28. Köhler, T.; Feoktystov, A.; Petracic, O.; Kentzinger, E.; Bhatnagar-Schöffmann, T.; Feygenson, M.; Nandakumaran, N.; Landers, J.; Wende, H.; Cervellino, A.; et al. Mechanism of Magnetization Reduction in Iron Oxide Nanoparticles. *Nanoscale* **2021**, *13*, 6965–6976, doi:10.1039/d0nr08615k.
29. Jefremovas, E.M.; Adams, M.P.; Gandarias, L.; Marcano, L.; Alonso, J.; Michels, A.; Leliaert, J. Micromagnetic Structure of Oxidized Magnetite Nanoparticles: Sharp Structural versus Diffuse Magnetic Interface. *Nanoscale* **2025**, *17*, 26203–26213, doi:10.1039/d5nr02700d.
30. Zákutná, D.; NiŽňanský, D.; Barnsley, L.C.; Babcock, E.; Salhi, Z.; Feoktystov, A.; Honecker, D.; Disch, S. Field Dependence of Magnetic Disorder in Nanoparticles. *Phys. Rev. X* **2020**, *10*, 1–17, doi:10.1103/PhysRevX.10.031019.
31. Zhu, S.; Fu, J.; Li, H.; Zhu, L.; Hu, Y.; Xia, W.; Zhang, X.; Peng, Y.; Zhang, J. Direct Observation of Magnetocrystalline Anisotropy Tuning Magnetization Configurations in Uniaxial Magnetic Nanomaterials. *ACS Nano* **2018**, *12*, 3442–3448, doi:10.1021/acsnano.8b00058.
32. Golosovsky, I. V.; Kibalin, I.A.; Liguori, D.; Muzzi, B.; Roca, A.G.; Lelièvre-Berna, E.; Puente-Orench, I.; Gukasov, A.; Nogués, J.; López-Ortega, A. Qualitative Evaluation of the Magnetocrystalline Anisotropy in Spinel Ferrite Nanoparticles Using Polarized Neutron Powder Diffraction. *Small* **2026**, 1–12, doi:10.1002/smll.73648.
33. Omelyanchik, A.; Villa, S.; Singh, G.; Rodionova, V.; Laureti, S.; Canepa, F.; Peddis, D. Magnetic Properties of Bi-Magnetic Core/Shell Nanoparticles: The Case of Thin Shells. *Magnetochemistry* **2021**, *7*, 146, doi:10.3390/magnetochemistry7110146.
34. Oberdick, S.D.; Abdelgawad, A.; Moya, C.; Mesbahi-Vasey, S.; Kepaptsoglou, D.; Lazarov, V.K.; Evans, R.F.L.; Meilak, D.; Skoropata, E.; van Lierop, J.; et al. Spin Canting across Core/Shell Fe3O4/MnxFe3−xO4 Nanoparticles. *Sci. Rep.* **2018**, *8*, 3425, doi:10.1038/s41598-018-21626-0.
35. Balaev, D.A.; Semenov, S. V.; Dubrovskii, A.A.; Krasikov, A.A.; Popkov, S.I.; Yakushkin, S.S.; Kirillov, V.L.; Mart'yanov, O.N. Synthesis and Magnetic Properties of the Core–Shell Fe3O4/CoFe2O4 Nanoparticles. *Phys. Solid State* **2020**, *62*, 285–290, doi:10.1134/S1063783420020043.
36. Herzer, G. The Random Anisotropy Model: Properties and Applications of Nanocrystalline Alloys from Amorphous Precursors. **2005**, *184*, 15–34.
37. Knobel, M.; Nunes, W.C.; Socolovsky, L.M.; De Biasi, E.; Vargas, J.M.; Denardin, J.C. Superparamagnetism and Other Magnetic Features in Granular Materials: A Review on Ideal and Real Systems. *J. Nanosci. Nanotechnol.* **2008**, *8*, 2836–2857, doi:https://doi.org/10.1166/jnn.2008.017.
38. Nunes, W.C.; Socolovsky, L.M.; Denardin, J.C.; Cebollada, F.; Brandl, A.L.; Knobel, M. Role of Magnetic Interparticle Coupling on the Field Dependence of the Superparamagnetic Relaxation Time. *Phys. Rev. B* **2005**, *72*, 212413, doi:10.1103/PhysRevB.72.212413.
39. Knobel, M.; Nunes, W.C.; Winnischofer, H.; Rocha, T.C.R.; Socolovsky, L.M.; Mayorga, C.L.; Zanchet, D. Effects of Magnetic Interparticle Coupling on the Blocking Temperature of Ferromagnetic Nanoparticle Arrays. *J. Non. Cryst. Solids* **2007**, *353*, 743–747, doi:10.1016/j.jnoncrysol.2006.12.037.
40. Balaev, D.A.; Semenov, S. V.; Dubrovskiy, A.A.; Yakushkin, S.S.; Kirillov, V.L.; Martyanov, O.N. Superparamagnetic Blocking of an Ensemble of Magnetite Nanoparticles upon Interparticle Interactions. *J. Magn. Magn. Mater.* **2017**, *440*, 199–202, doi:10.1016/j.jmmm.2016.12.046.
41. Sánchez, E.H.; Vasilakaki, M.; Lee, S.S.; Normile, P.S.; Muscas, G.; Murgia, M.; Andersson, M.S.; Singh, G.; Mathieu, R.; Nordblad, P.; et al. Simultaneous Individual and Dipolar Collective Properties in Binary Assemblies of Magnetic Nanoparticles. *Chem. Mater.* **2020**, *32*, 969–981, doi:10.1021/acs.chemmater.9b03268.
42. Muscas, G.; Concas, G.; Laureti, S.; Testa, A.M.; Mathieu, R.; De Toro, J.A.; Cannas, C.; Musinu, A.; Novak, M.A.; Sangregorio, C.; et al. The Interplay between Single Particle Anisotropy and Interparticle Interactions in Ensembles of Magnetic Nanoparticles. *Phys. Chem. Chem. Phys.* **2018**, *20*, 28634–28643, doi:10.1039/c8cp03934h.
43. Muscas, G.; Jovanović, S.; Vukomanović, M.; Spreitzer, M.; Peddis, D. Zn-Doped Cobalt Ferrite: Tuning the Interactions by Chemical Composition. *J. Alloys Compd.* **2019**, *796*, 203–209, doi:10.1016/j.jallcom.2019.04.308.
44. Savin, V.P.; Koksharov, Y.A. Screening Effect of a Magnetically Soft Shell of Single-Domain Ferromagnetic Nanoparticles. *J. Magn. Magn. Mater.* **2025**, *630*, 173473, doi:10.1016/j.jmmm.2025.173473.
45. Trohidou, K.N.; Soukoulis, C.M.; Kostikas, A.; Hadjipanayis, G. Size Dependence of Coercivity of Small Magnetic Particles. *J. Magn. Magn. Mater.* **1992**, *104–107*, 1587–1588, doi:10.1016/0304-8853(92)91465-6.

46. Yoon, S.; Krishnan, K.M. Temperature Dependence of Magnetic Anisotropy Constant in Manganese Ferrite Nanoparticles at Low Temperature. *J. Appl. Phys.* **2011**, *109*, 2009–2012, doi:10.1063/1.3563068.
47. Omelyanchik, A.; Villa, S.; Vasilakaki, M.; Singh, G.; Ferretti, A.M.; Ponti, A.; Canepa, F.; Margaris, G.; Trohidou, K.N.; Peddis, D. Interplay between Inter- And Intraparticle Interactions in Bi-Magnetic Core/Shell Nanoparticles. *Nanoscale Adv.* **2021**, *3*, 6912–6924, doi:10.1039/d1na00312g.
48. Sanna Angotzi, M.; Mameli, V.; Cara, C.; Musinu, A.; Sangregorio, C.; Niznansky, D.; Xin, H.L.; Vejpravova, J.; Cannas, C. Coupled Hard–Soft Spinel Ferrite-Based Core–Shell Nanoarchitectures: Magnetic Properties and Heating Abilities. *Nanoscale Adv.* **2020**, *2*, 3191–3201, doi:10.1039/D0NA00134A.
49. Sartori, K.; Lopez-Martin, R.; Choueikani, F.; Gloter, A.; Grenèche, J.M.; Begin-Colin, S.; Taverna, D.; De Toro, J.A.; Pichon, B.P. Magnetic Anisotropy Engineering in Onion-Structured Metal Oxide Nanoparticles Combining Dual Exchange Coupling and Proximity Effects. *Nanoscale Adv.* **2024**, *6*, 2903–2918, doi:10.1039/d3na01108a.
50. Lavorato, G.; Winkler, E.; Rivas-Murias, B.; Rivadulla, F. Thickness Dependence of Exchange Coupling in Epitaxial Fe3O4/CoFe2O4 Soft/Hard Magnetic Bilayers. *Phys. Rev. B* **2016**, *94*, 054405, doi:10.1103/PhysRevB.94.054405.
51. Poon, K.; Gupta, A.; Hawkins, P.M.E.; Singh, G. Core-Shell Magnetic Nanoparticles : Harnessing Synergistic Effects for MRI and Magnetic Hyperthermia. *Mater. Today Chem.* **2025**, *44*, 102533, doi:10.1016/j.mtchem.2025.102533.
52. Liébana-Viñas, S.; Simeonidis, K.; Wiedwald, U.; Li, Z.-A.A.; Ma, Z.; Myrovali, E.; Makridis, A.; Sakellari, D.; Vourlias, G.; Spasova, M.; et al. Optimum Nanoscale Design in Ferrite Based Nanoparticles for Magnetic Particle Hyperthermia. *RSC Adv.* **2016**, *6*, 72918–72925, doi:10.1039/C6RA17892H.
53. Sandler, S.E.; Fellows, B.D.; Mefford, O.T. Best Practices for Characterization of Magnetic Nanoparticles for Biomedical Applications. *Anal. Chem.* **2019**, *91*, 14159–14169, doi:10.1021/acs.analchem.9b03518.
54. Omelyanchik, A.; Muscas, G.; Peddis, D. Magnetic Correlation Length in Hard/Soft Core–Shell Magnetic Nanoarchitectures [Data Set]., doi:10.5281/zenodo.17941186.
55. Livesey, K.L.; Ruta, S.; Anderson, N.R.; Baldomir, D.; Chantrell, R.W.; Serantes, D. Beyond the Blocking Model to Fit Nanoparticle ZFC/FC Magnetisation Curves. *Sci. Rep.* **2018**, *8*, 1–9, doi:10.1038/s41598-018-29501-8.
56. Coey, J.M.D. *Magnetism and Magnetic Materials*; Cambridge University Press, 2010;
57. Concas, G.; Congiu, F.; Muscas, G.; Peddis, D. Determination of Blocking Temperature in Magnetization and Mössbauer Time Scale: A Functional Form Approach. *J. Phys. Chem. C* **2017**, *121*, 16541–16548, doi:10.1021/acs.jpcc.7b01748.
58. Komogortsev, S. V.; Stolyar, S. V.; Mokhov, A.A.; Fel'k, V.A.; Velikanov, D.A.; Iskhakov, R.S. Effect of the Core–Shell Exchange Coupling on the Approach to Magnetic Saturation in a Ferrimagnetic Nanoparticle. *Magnetochemistry* **2024**, *10*, doi:10.3390/magnetochemistry10070047.
59. Akulov, N.S. Uber Den Verlauf Der Magnetisierungskurve in Starken Feldern. *Zeitschrift fur Phys.* **1931**, *69*, 822–831, doi:10.1007/BF01339465.
60. Omelyanchik, A.; Salvador, M.; D'Orazio, F.; Mameli, V.; Cannas, C.; Fiorani, D.; Musinu, A.; Rivas, M.; Rodionova, V.; Varvaro, G.; et al. Magnetocrystalline and Surface Anisotropy in CoFe2O4 Nanoparticles. *Nanomaterials* **2020**, *10*, 1–11, doi:10.3390/nano10071288.
61. El-Hilo, M. Nano-Particle Magnetism with a Dispersion of Particle Sizes. *J. Appl. Phys.* **2012**, *112*, 103915, doi:10.1063/1.4766817.
62. Néel, L. Some Theoretical Aspects of Rock-Magnetism. *Adv. Phys.* **1955**, *4*, 191–243, doi:10.1080/00018735500101204.
63. Brown, W.F. Thermal Fluctuations of a Single-Domain Particle. *Phys. Rev.* **1963**, *130*, 1677–1686, doi:10.1103/PhysRev.130.1677.
64. Zélis, P.M.; Bruvera, I.J.; Calatayud, M.P.; Goya, G.F.; Sánchez, F.H. Determination of the Blocking Temperature of Magnetic Nanoparticles: The Good, the Bad and the Ugly. *J. Appl. Phys.* **2015**, *118*, 184304, doi:10.1063/1.4935484.
65. Cannas, C.; Musinu, A.; Piccaluga, G.; Fiorani, D.; Peddis, D.; Rasmussen, H.K.; Mørup, S. Magnetic Properties of Cobalt Ferrite–Silica Nanocomposites Prepared by a Sol-Gel Autocombustion Technique. *J. Chem. Phys.* **2006**, *125*, 164714, doi:10.1063/1.2354475.
66. Margaris, G.; Trohidou, K.N.; Nogués, J. Mesoscopic Model for the Simulation of Large Arrays of Bi-Magnetic Core/Shell Nanoparticles. *Adv. Mater.* **2012**, *24*, 4331–4336, doi:10.1002/adma.201200615.
67. Ping Liu, J.; Gutfleisch, O.; Fullerton, E.; Sellmyer, D.J. *Nanoscale Magnetic Materials and Applications*; Liu, J.P., Fullerton, E., Gutfleisch, O., Sellmyer, D.J., Eds.; Springer US: Boston, MA, 2009; ISBN 9780387855981.
68. Lavorato, G.; Alzamora, M.; Contreras, C.; Burlandy, G.; Litterst, F.J.; Baggio-Saitovitch, E. Internal

Structure and Magnetic Properties in Cobalt Ferrite Nanoparticles: Influence of the Synthesis Method. *Part. Part. Syst. Charact.* **2019**, *36*, 1–11, doi:10.1002/ppsc.201900061.

69. Balaev, D.A.; Poperechny, I.S.; Krasikov, A.A.; Semenov, S. V.; Popkov, S.I.; Knyazev, Y. V.; Kirillov, V.L.; Yakushkin, S.S.; Martyanov, O.N.; Raikher, Y.L. Dynamic Remagnetisation of CoFe 2 O 4 Nanoparticles: Thermal Fluctuational Thawing of Anisotropy. *J. Phys. D. Appl. Phys.* **2021**, *54*, 275003, doi:10.1088/1361-6463/abf371.
70. López-Ortega, A.; Lottini, E.; Fernández, C.D.J.; Sangregorio, C. Exploring the Magnetic Properties of Cobalt-Ferrite Nanoparticles for the Development of a Rare-Earth-Free Permanent Magnet. *Chem. Mater.* **2015**, *27*, 4048–4056, doi:10.1021/acs.chemmater.5b01034.
71. Song, Q.; Zhang, Z.J. Controlled Synthesis and Magnetic Properties of Bimagnetic Spinel Ferrite CoFe 2O 4 and MnFe 2O 4 Nanocrystals with Core-Shell Architecture. *J. Am. Chem. Soc.* **2012**, *134*, 10182–10190, doi:10.1021/ja302856z.